








RESEARCH ARTICLE OPEN ACCESS

Advanced Photoluminescence Imaging Method for Robust and Scalable Perovskite Quality Monitoring in Monolithic Tandem Solar Cells

Julian Petermann¹  | Benjamin Hacene²  | Mohammad Gholipour¹  | Felix Laufer²  | Raphael Pesch¹  | Xuzheng Liu¹  | Ulrich Wilhelm Paetzold^{1,2} 

¹Institute of Microstructure Technology (IMT), Karlsruhe Institute of Technology (KIT), Eggenstein-Leopoldshafen, Germany | ²Light Technology Institute (LTI), Karlsruhe Institute of Technology (KIT), Karlsruhe, Germany

Correspondence: Ulrich Wilhelm Paetzold (ulrich.paetzold@kit.edu)

Received: 24 March 2025 | **Revised:** 8 May 2025 | **Accepted:** 9 May 2025

Keywords: imaging | perovskite | photoluminescence | solar cells | tandem

ABSTRACT

Photoluminescence-based characterization techniques are widely employed in perovskite solar cell research, offering a noninvasive and contactless means of obtaining information about the implied open-circuit voltage (iV_{oc}) and, hence, the absorber quality. Driven by the idea of developing a robust yet quantitative in-line imaging method for perovskite/Si tandem solar cells, we have extended an intensity-dependent photoluminescence method initially reported for single-junction solar cells. This method enables local quality assessment of the perovskite thin-film absorbers processed over planar and textured silicon bottom solar cells with high spatial resolution. A single effective parameter k , also called optical ideality factor, is extracted, which accounts for the complex superposition of locally competing recombination processes. This work demonstrates that our method, called k -imaging, is a robust and versatile characterization tool for perovskite/Si tandem solar cells that allows the assessment of the general thin-film absorber quality as well as of specific defects for both scientific and industrial applications. Consequently, it accelerates perovskite research and paves the way for highly reproducible perovskite deposition processes toward commercialized perovskite/Si tandem solar cells.

1 | Introduction

Photovoltaics (PV) has evolved into a mature renewable energy technology, which bears the potential to cover a large fraction of the world's electrical demand by harvesting the virtually inexhaustible resource of the sun. As established silicon PV technologies are approaching their theoretical power conversion efficiency (PCE) limit around 29.5% [1], researchers globally search for new PV technologies and materials. In recent years perovskite solar cells (PSC) have generated particular interest from industry and research [2].

Metal halide perovskite (Pero) semiconductors are a low-cost material class with excellent optoelectronic properties such as

high absorption, long carrier diffusion lengths, and a widely tunable bandgap [3–6]. For these reasons, this material class contains many candidates that appear perfectly suited for the next-generation thin-film solar cells. In particular, so-called perovskite/Si tandem solar cells promise high performance with only a moderate cost increase compared to established silicon single-junction PV technologies [3]. Laboratory-scale perovskite/Si tandem solar cells currently yield a PCE of up to 34.6%, which significantly exceeds the limit of single-junction silicon solar cells [7]. However, realizing such outstanding performance at the module scale is, in part, held back by the practical challenge of producing uniform high-quality perovskite layers onto silicon subcells on full wafer scale [2, 8]. Perovskite thin films are polycrystalline and mechanically soft, exhibiting high

This is an open access article under the terms of the [Creative Commons Attribution](https://creativecommons.org/licenses/by/4.0/) License, which permits use, distribution and reproduction in any medium, provided the original work is properly cited.

© 2025 The Author(s). *Solar RRL* published by Wiley-VCH GmbH.

defect concentrations if not processed at optimal conditions [9, 10]. Viable coating techniques for implementation in industrial production are thermal evaporation [11, 12], inkjet printing [13–15], blade coating [15, 16], slot-die coating [17, 18], and spray coating [19, 20]. While these are considered promising for upscaling, each one also exhibits specific challenges with regard to defect susceptibility, layer thickness uniformity, or compositional homogeneity [21]. Regardless of the prevailing technique, monolithic perovskite/Si tandem solar cells involve numerous production steps, with the perovskite coating being one of the final and most critical steps. High production yield for the perovskite thin film is of utmost importance, given that substantial financial efforts have been spent on the bottom cell already in the entire production chain. Therefore, monitoring of perovskite thin-film quality in tandem solar cell production is essential in order to minimize production costs by achieving low rejection rates [22, 23].

Noninvasive photoluminescence (PL)-based techniques are ideal for in-line inspection as the PL provides immediate insights into the charge carrier dynamics and thin-film quality (i.e., the PL correlates with the open-circuit voltage V_{oc}) [24, 25]. Moreover, PL analysis provides insights into the absorber layer quality even before completion of the solar cell device stack [24–26]. Various PL-based characterization methods are used in the perovskite community, namely intensity- and voltage-dependent techniques combined with spatial, spectral, or temporal resolution [16, 25, 27–33].

Among the PL-based thin-film quality analysis methods, the photoluminescence quantum yield (PLQY) provides the highest level of insight as it correlates to the absolute quasi-Fermi-level splitting and iV_{oc} [24]. In perovskite/Si tandem solar cells, however, a major proportion (~85%) of the perovskite PL emission is absorbed by the Si bottom cell [34], which results in a substantial underestimation of the PLQY if the same calibration routines are applied as for perovskite thin films in single-junction solar cells. As a consequence, there is no direct differentiation whether a decrease in PLQY is caused by a deterioration in perovskite quality or by a beneficial enhancement in photon trapping. This systematic error inherent to tandem cells undermines its key advantage over noncalibrated systems. Furthermore, the necessity for laser excitation and an integrating sphere prevents its implementation in situ and restricts it to spatially integrated information. In contrast, PL imaging is a straightforward and versatile technique to extract the local PL intensity. It is suitable for large-scale implementation as it relies exclusively on cost-efficient, commercially available, and fully modular industrial machine vision components, such as light-emitting diodes (LED) elements and conventional cameras [31]. However, to date, the interpretation is challenging due to a lack of quantitative information. Ambiguous effects can be misinterpreted easily, as, for example, high PL intensity can be caused by high absorber quality or by highly scattering thin-film regions.

In response, Hacene et al. introduced the method of k -imaging for single-junction PSCs, which enables the generation of a quantitative quality metric while maintaining the versatility and scalability of PL imaging [29]. This method employs intensity-dependent PL imaging to extract information about the local dominating charge recombination processes. Other methods that

investigate the recombination processes are generally based on time-resolved measurements, which usually do not offer spatial resolution at all or involve time-consuming scanning methods. Following this methodology offers unique features including its noninvasive nature, in-line applicability, and robustness. In detail, the parameter k exclusively represents the intensity dependence but is independent of constant optical effects, which can differ drastically between and across samples. The most relevant types of such artifacts are morphology-induced outcoupling variances, especially common for solution-processed thin films. When comparing different architectures, also substantial stack-specific absorption occurs mainly by sub-cells but also various other interlayers. Finally, it also eliminates moderate spatial variations in the excitation and the detection window which means advanced calibrations are not required. We refined the original methodology by including interface recombination into the interpretation and extended its applicability to planar and textured perovskite/Si tandem solar cells. This transfer, however, is not trivial due to the dramatic decrease in outcoupled perovskite PL while irrelevant PL emission originating from the Si bottom cell appears and potentially interferes with the measurement [34]. In more detail, the Si cell, as the material with the highest refractive index, absorbs most of the perovskite PL emission and re-emits it at its characteristic wavelength. This is amplified even more when textured bottom cells facilitate light trapping by internal reflections. Another result of these reflections is the certain randomization of out-coupling angles, while the detection cone is restricted by the camera and lens positioning.

Overall, the method offers unique features, including its noninvasive nature, in-line applicability, and robustness, making it ideal for industrial quality monitoring. In addition, the evaluation of thin-film quality with spatial resolution is a valuable tool for process optimization and stability testing in academic research as well.

2 | Results and Discussion

2.1 | Methodology

In pursuit of developing a noninvasive and robust in-line imaging method that locally resolves the quality of the perovskite thin-film absorber processed over a silicon bottom solar cell with high spatial resolution, in this work, we advance the previously introduced k -imaging method to the demanding case of tandem solar cells [29]. This method accounts for the complex superposition of competing recombination processes by extracting a single effective parameter k , using a basic recombination model $I_{PL} \approx I_{exc}^k$ on intensity-dependent and spatially resolved photoluminescence data.

2.1.1 | Model Fundamentals

To shed some light on the underlying concept, this k -imaging method is motivated from fundamental rate laws of excitation and recombination. The general dynamics of the charge carrier density n in the perovskite thin film are described by the rate law:

$$\frac{dn}{dt} = eI_{\text{exc}} - an - bn^2 - cn^3 \quad (1)$$

where eI_{exc} is the generation of charge carriers by photoexcitation and a , b , c are the rate constants for the respective fundamental recombination process [35, 36]. The exponent of n in Equation (1) relates to the recombination order, i.e., the number of free charge carriers involved in the respective mechanism discussed below.

In this model, the nonradiative trap-assisted recombination in the bulk, also Shockley–Read–Hall (SRH) recombination, is expressed by the first-order term with the rate constant a , as only one charge carrier interacts with a constant number of intragap defect states. The origin of second-order recombination is not monocausal but occurs from both radiative bulk and nonradiative interface recombination. First, radiative band-to-band bulk recombination is the inverse equivalent of photon-excited carrier generation. For that reason, at open circuit where charge extraction is not possible, high radiative recombination is desired and a sign of good absorber quality [25]. However, nonradiative trap-assisted interface recombination also exhibits an approximately second-order mechanism. This process is more complex depending not only on the interfacial trap density but also on the charge carrier asymmetry and the misalignment of bands at the interface. Simplified, it is considered as a nonradiative bimolecular recombination, leading to a potentially ambiguous interpretation of any second-order recombination [37, 38]. This contribution is regularly disregarded when interpreting recombination rate laws, also in the publication by Hacene et al. but it is reported to have a major impact if interfaces, especially unoptimized or unintended ones, are involved [39]. The last, third-order term

with constant c , related to Auger recombination, is irrelevant for perovskites at the relatively low intensities applied with our method (<1 sun) and, therefore, can be neglected in our model [40].

In steady state, the differential equation simplifies to a direct relation between excitation intensity and charge carrier density [35]:

$$eI_{\text{exc}} = an + bn^2 \quad (2)$$

Further, PL is emitted by radiative band-to-band recombination, hence described as:

$$I_{\text{PL}} = b_{\text{rad}}n^2 \quad (3)$$

By combining Equations, (2) and (3), the power law in Equation (4) can be derived between excitation and PL intensity with k being the exponent.

$$I_{\text{PL}} \sim I_{\text{exc}}^k \quad (4)$$

Resulting from the recombination conditions described above, this parameter ranges between 1 and 2. It can change over many magnitudes of excitation intensity, however, with our experimental conditions it can be considered constant due to a relatively limited excitation range of less than two magnitudes [35]. It is to note that k is not equivalent to the recombination rate order or any other physical quantity but combines the discussed processes in a single effective parameter, giving insight into the local dominating recombination (Figure 1a). If SRH recombination is dominant, k tends toward 2, while both radiative band-to-band

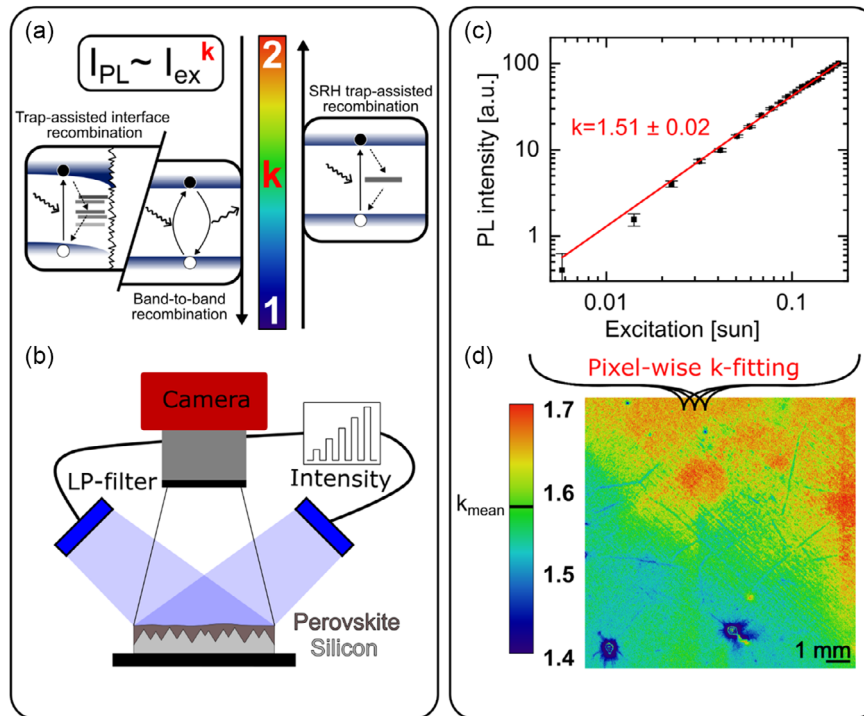


FIGURE 1 | Fundamental method representation and practical procedure of k -imaging. (a) Relevant recombination paths, i.e., interface trap-assisted, band-to-band, and Shockley–Read–Hall trap-assisted recombination and their effect on the local power-law factor k . (b) Excitation intensity-dependent photoluminescence imaging of an exemplary level perovskite on textured silicon half stack (ii). (c) Determination of local k by pixel-wise power-law fitting and (d) aggregation to a full image.

recombination and interfacial recombination push k toward 1. This parameter k reminds of the closely related and widely used diode ideality factors, with a few systematic differences.

2.1.2 | Recapitulation and Differentiation of Related Diode Ideality Factors

In addition to its fundamental derivation from recombination rate laws, the parameter k is the purely optical and spatially resolved equivalent of the external diode ideality factor n_{ext} in the absence of charge extraction, i.e., contacts, which is a well-established parameter included in the simplified classical diode equation in open-circuit condition (Equation (5))

$$J_{\text{R}} = J_0 \exp\left(\frac{qV_{\text{OC}}}{n_{\text{ext}}k_{\text{B}}T}\right) \quad (5)$$

where J_{R} is the recombination current, J_0 is the dark recombination current, q is the carrier charge, V_{OC} is the open-circuit voltage, and $k_{\text{B}}T$ the thermal energy [41]. This parameter n_{ext} extends the ideal diode theory to reality where nonideal recombination cannot be neglected and n_{ext} deviate from unity. Typical recombination processes and their resulting ideality factors are the same as for k , discussed above. While the external diode ideality factor is common in theoretical models, practically it requires electrical measurements on a fully contacted device. In contrast, the internal ideality factor n_{int} is more frequently used as it can be determined already for incomplete devices and even single-absorber layers, based on the optically measured implied open-circuit voltages iV_{OC} , which represent the photoelectrochemical limit, based on the ideal, fully radiative implied voltage $iV_{\text{OC,rad}}$ (Equation (6)) [28, 42].

$$iV_{\text{OC}} = iV_{\text{OC,rad}} + k_{\text{B}}T \ln(\text{PLQY}) \quad (6)$$

n_{int} is then fitted similarly to the diode equation in Equation (5), but using intensity-dependent implied open-circuit voltages iV_{OC} [28, 43].

$$J_{\text{R}} = J_0 \exp\left(\frac{qiV_{\text{OC}}}{n_{\text{int}}k_{\text{B}}T}\right) \quad (7)$$

Naturally, the internal ideality factor is based on the present, potentially incomplete interfaces, which causes a systematic difference between n_{int} and n_{ext} if other relevant interfaces and following recombination mechanisms are introduced upon device completion. While the determination of the intermediate iV_{OC} relies on calibrated photon intensities, direct fitting of n_{int} is also possible, which opens the possibility of measuring it even with noncalibrated PL imaging. Using the criteria of open-circuit operation, we end up at the widely observed power-law relation between integrated PL intensity I_{PL} and excitation I_{exc} .

$$I_{\text{PL}} \sim J_{\text{rad}} \sim J_0 \exp\left(\frac{qiV_{\text{OC}}}{k_{\text{B}}T}\right) = J_{\text{R}}^{n_{\text{int}}} \sim I_{\text{exc}}^{n_{\text{int}}} \quad (8)$$

In our method, we take this one step further and apply this law to spatially resolved PL maps while the original Equation (8) is strictly true only if the electrochemical potential $\mu = qiV_{\text{OC}}$, which

was reported to be reasonable if spatial averages are taken [5, 44]. To highlight this difference, we refer to this exponent as k instead of n_{int} , in literature also called optical ideality factor and end up at the simple model (Equation (4)) our method is based on [4]. Overall, k -imaging has the potential to substitute the most rigorous optoelectronic metric, which is PLQY, for applications where its usage is technically not feasible or PLQY cannot maintain its absolute meaning due to secondary absorption in tandem solar cells.

Last, we want to note that this fitting model is valid also for other semiconductor materials, provided the fundamental rate laws are applicable [29, 36, 43]. However, even in case of additional rate-law consistent mechanisms like Auger recombination, the interpretable range of k needs a specific modification.

2.1.3 | Experimental Approach

To investigate defects and inhomogeneities in perovskite thin films, a measurement setup was developed to record the spatially resolved and intensity-dependent PL images, which the k parameter is derived from. The setup consists of two tilted, intensity-controllable LED bars (470 nm) to excite the perovskite side of the tandem half-stack homogeneously (Figure 1b). The electron-hole pairs created by the absorption of these highly energetic photons cannot be extracted in the given open-circuit conditions and, therefore, recombine through one of the described recombination channels. The resulting PL signal, emitted from the perovskite, is recorded by a camera equipped with a suitable long-pass filter to eliminate the residual excitation signal, see details in Figure S1, Supporting Information. The PL dataset is recorded by performing an intensity sweep from about 0.005 to 0.2 sun equivalents. As only the model exponent k is relevant for the method, a relative determination of the incident excitation suffices. For that reason, the absolute absorbed excitation intensity is interesting for the context but not required to determine k . To correct for stray light and a camera-related baseline signal, a simple background correction at zero excitation is implemented. Finally, the k factors are fitted for each image pixel by applying our model in Equation (4) and assembled in one k -image (Figure 1c,d).

2.2 | k -Imaging in Perovskite/Si Tandem Solar Cells

In the following, the applicability and versatility of k -imaging applied to perovskite thin films is shown for perovskite/Si tandem solar cells. Hacene et al. demonstrated the value of k -imaging in the context of perovskite single-junction half-stacks. In this work, we extend this approach to application on perovskite/Si tandem half stacks. To demonstrate its value for both academia and industry, we present the method based on the three most relevant perovskite-silicon stacks. Those include (i) planar perovskite thin film on planar Si-subcell, (ii) level (valley-filling) perovskite on textured Si-subcell, and (iii) conformal perovskite on textured Si-subcell (Figure 2a–c). In particular, compatibility of this method with textured substrates is a key feature as these are the standard for industrial solar cells. To emphasize the relevance and quality of the presented half stacks,

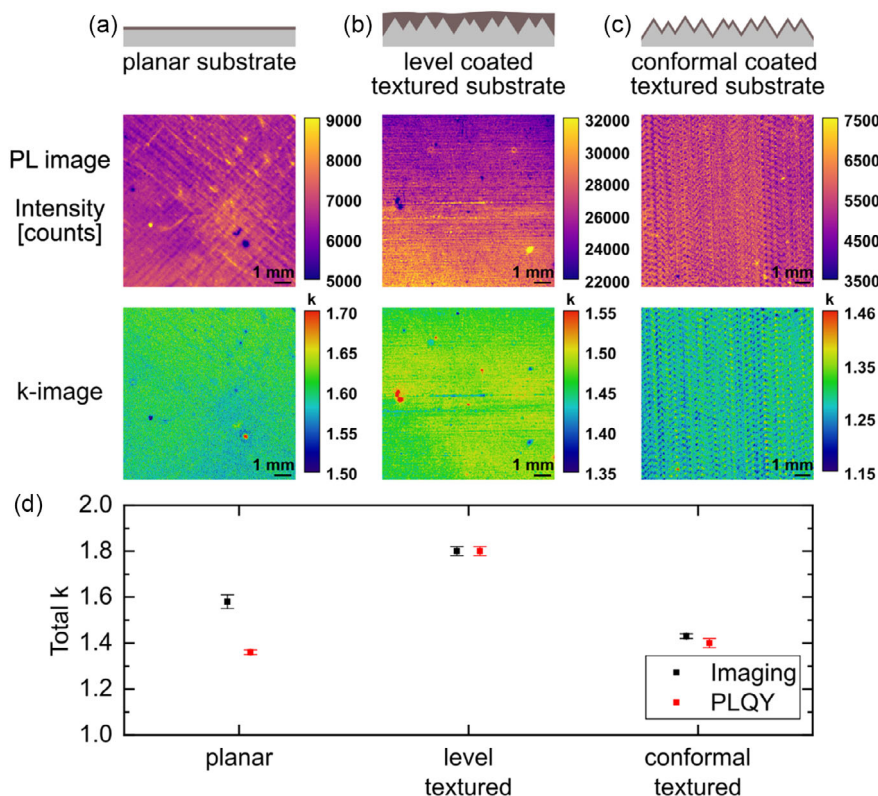


FIGURE 2 | Schematic tandem morphology, exemplary photoluminescence image and k -image for the tandem stack types, (a) planar perovskite thin film on planar Si-subcell, (b) level perovskite on textured Si subcell, and (c) conformal perovskite on textured Si subcell. (d) Correlation between spatially integrated k factor measured with the k -imaging method and via photoluminescence quantum yield (different set of cells).

we show representative device performance data in Figure S2, Supporting Information

2.2.1 | Robustness

The strength of k -imaging is its foundation on local, intensity-dependent fitting instead of absolute PL intensities. This approach results in robustness against constant spatial variation in the optical in- and out-coupling. That includes varying reflectivity due to roughness and texture as well as slightly nonuniform incident excitation intensity. This contrasts with basic PL imaging, which is unable to differentiate between variation in the materials PL response and unrelated optical influences.

A prominent example is shown in Figure 2a, where the PL image demonstrates diagonal lines of significantly increased intensity, while the k -factor indicates that there is barely any influence on the recombination. The line structure is caused by superficial processing defects in the planar Si surface, modifying the local optical reflection, but not influencing the quality of the perovskite layer. Moreover, Figure 2b shows a measurement influenced by a vertical gradient in the incident excitation leading to a corresponding gradient in the PL image with significant variation of almost 50%. Nonetheless, the corresponding k -image is unaffected for a wide range of variations. The resulting k -image might only be impacted if the spatial excitation varies over an order of magnitude as the overall recombination mechanism might not remain constant. Besides optical effects, level-coated textures also include substantial perovskite layer thickness variations. The resulting thickness

typically ranges from 100 nm to 1 μ m and occurs laterally within the texture dimensions of about one micrometer [45]. Since our imaging system is limited to a maximum pixel resolution of $5 \times 5 \mu\text{m}^2$, these variations cannot be resolved with our setup, i.e., any potential impacts on k are averaged over many pyramid dimensions. However, if a sufficient submicron resolution is achieved, we expect an observable effect on k . In Figure 2c a conformally coated perovskite thin film is shown. The thin film was fabricated using a hybrid two-step process consisting of evaporation of the inorganics and inkjet printing of the organic cation precursor. Both PL-image and k -image show a regular pattern across the sample. It is to be noted that this pattern is unrelated to the textures. Instead, it is a printing pattern that emerges from a combination of the specific sequential droplet deposition during organic precursor printing and uneven organic deposition upon drying of the individual ink droplets (coffee ring effect) [13]. After the evaporation of the droplet's solvent, this phenomenon creates a ring-shaped concentration gradient on the surface [46]. Due to the limited mobility of the organic species, local organic excess remains on the surface and changes the local recombination in particular at the surface. The presence of this pattern indicates inhomogeneous surficial cation distribution, leading to a variation in the perovskite quality. Identification and quantification of such variation is essential for the optimization of process parameters. This example highlights why imaging is an essential capability, not only for detecting random defects but also for systematic, in this case periodic, layer quality variations that could not be detected with single-spot measurements.

2.2.2 | Validation

While direct correlation between the final device performance and k as an indicator for perovskite thin-film quality seems to be the most straightforward approach, it would be of quite limited use and is quite challenging to interpret. The major limitation is the essential and systematic difference between evaluating the spatially resolved optoelectronic quality of the perovskite absorber and the total operational performance of the full device. First, the detrimental implication of a specific defect or local variation is not necessarily apparent in the integrated device's performance, if other more significant defects in the absorber are limiting device performance. Second, the optical ideality factor k is inherently limited to the absorber and potentially neighboring charge transport interfaces while the performance represents a more complex full stack with additional layers and interfaces. Finally, the methodology of k -imaging is based on an open-circuit condition, i.e., in the absence of any charge extraction. That as well can lead to defects, inarguably being very prominent in open circuit upon charge accumulation but much less significant when fast charge extraction is present. Nonetheless, by focusing on specific recombination mechanisms, Hacene et al. and Babbe et al. confirmed that the optical ideality factor k indeed reflects systematic changes in recombination or even device parameters [29, 43].

Further, we validate the compatibility of our method with tandem solar cells by comparison of our imaging-derived total k with measurements using the most rigorous reference, which is a state-of-the-art PLQY system. Although the PLQY is only determined as a spatial integral, it provides higher global accuracy due to angular integration and spectral resolution, shown by the example in Figure S3, Supporting Information.

The comparison in Figure 2d shows an excellent agreement in the case of level and conformally coated perovskite on textured Si substrates. Due to the randomization of light paths in these substrates the intensity-dependent PL emission and the derived local k agree very well with values obtained from PLQY measurements. For planar cells, however, there is a significant deviation in the absolute value of k ($\Delta k = 0.22$) extracted by the imaging setup and the PLQY system. It is important to note that this difference is not relevant for the qualitative assessment of perovskite thin films but only refers to the absolute value. We attribute the increased discrepancy in the absolute k to a prominent nonlinear characteristic, given that effects that are linear with regard to the excitation intensity should not affect the evaluation of the absolute value of k . The most apparent nonlinear effect that might be more pronounced in planar devices is photon recycling, which has a very prominent effect on single-junction half stacks on glass [47]. Even though it is greatly reduced in tandem solar cells as the Si bottom cell has the highest refractive index in the layer stack and absorbs most of the photons emitted, it is possibly more relevant in planar stacks where emitted photons can be guided horizontally in the device stack.

In conclusion, compared to plain PL imaging, k -imaging exhibits a notable resilience against fluctuations in optical out-coupling and excitation intensity. This presents a crucial benefit as it simplifies both the technical implementation and subsequent interpreta-

tion, thereby rendering it a robust and reliable characterization technique. Moreover, no fundamental applicability limitations have been observed or are expected for any combination of conventional substrate morphologies (e.g. texture) and perovskite deposition techniques.

2.3 | Robustness and Repeatability

To demonstrate the robustness and repeatability of the k -imaging method for a perovskite thin film on silicon bottom cells, continuous measurement series are performed on single tandem cells. Figure 3 exemplarily displays the results of a (ii) level perovskite thin film on a textured silicon bottom cell. Both the total k and the spatial variation and prominence of inhomogeneities show low variation. Also, two well-defined and systematically different measurement conditions are identified, hereafter referred to as a dark and soaked states.

The main prerequisite for the applicability of our model is the fundamental criterion that a (quasi-) steady-state is realized with respect to charge carrier density within each intensity step and to recombination channels throughout the entire measurement time. Any deviation from these assumptions would lead to a gradual systematic change in the perovskite, resulting in a distortion of the obtained k -factor. Two essential contributions are discussed: the roles of electrons and ions. The stability of the electronic steady state is justified since even long electron lifetimes ($<100 \mu\text{s}$) and the equilibration time derived from them are orders of magnitude shorter than the fastest possible response times of the excitation and acquisition control ($\sim 100 \text{ ms}$) [48]. Therefore, assuming stable recombination processes in the perovskite film, the assumption of an electronic equilibrium within each excitation step is valid. Second, measuring the k -factor is only meaningful if the recombination mechanisms stay consistent across all excitation steps. The effect of light soaking must be considered to ensure constant recombination conditions of the perovskite, as it can directly affect the presence of trap-assisted recombination. It has been widely reported that many trap states within the bandgap originate from ionic defects such as vacancies, interstitials, or charge accumulation at the interfaces [49]. Therefore, prolonged illumination alters the distribution and density of trap states, leading to a systematic change in carrier recombination behavior [50]. In agreement with previous reports, the recording of the soaking-dependent PL shows a significant increase in intensity and saturation after about 60 min (Figure S4a, Supporting Information) [50–52]. The analysis of the k -factor after different soaking times shows a similar trend with a high k (~ 1.8) at zero presoaking, defined as dark state, and an equalization to lower values (~ 1.4), defined as soaked state (Figure S4b, Supporting Information). Since light soaking has much longer response times compared to electron processes, these well-defined states can be systematically created by suitable presoaking.

The total k , shown in Figure 3a, demonstrates two separate and repeatable levels with a notable offset. The dark state measurements show a consistent k of about 1.72, indicating that nonradiative SRH recombination is dominant in this state. However, the k -factor of the soaked state is significantly reduced to about 1.41, indicating a reduced contribution of SRH recombination.

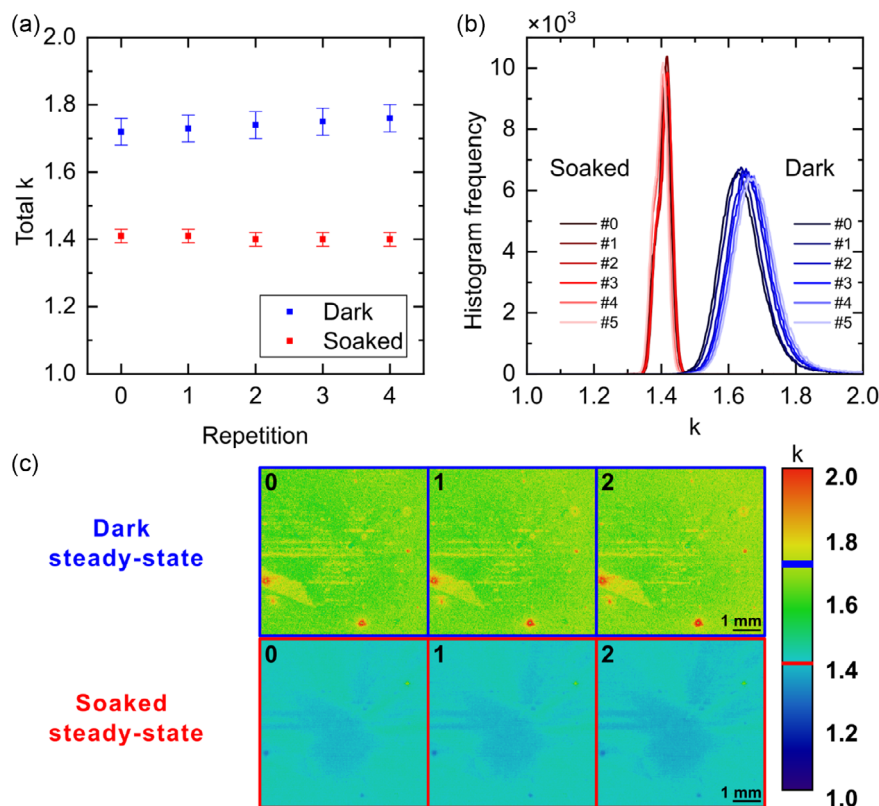


FIGURE 3 | Differentiation of light-soaked (60 min at max. intensity of 0.2 suns) and dark quasi-steady-state (no prior light soaking). A repeatability study is represented by (a) total k , (b) the distribution of k , and (c) the k -images in both states. The total k -factor and their errors are indicated in the color bar by markers of the respective color.

Those results fit well to the theory of reduced (or inactivated) defect state densities induced by light soaking [50]. It is also noticeable that the error bars of the dark series is consistently larger than those of the soaked series. The main reason is the higher PL signal, which leads to a lower statistical error. The saturated soaked PL signal is about six times higher, resulting in a higher signal-to-noise ratio. Another reason may be the increased overall variation within the k -image in the dark state, visualized by the greater width in the distribution of k (Figure 3b). However, measurements have shown that small sample variations only play a minor role in the total fit uncertainty compared to the effect of an improved signal level.

In addition to the change in the overall k -factor between the dark and soaked states, there is also a change in the prominence of defects and inhomogeneities (Figure 3c) and thus the overall distributional variance (Figure 3b). While the major defects can be identified in both conditions, the affected area of point defects becomes smaller and less pronounced. In addition, the overall distribution width is approximately halved after soaking, which complements the observation of decreasing spatial variance with respect to recombination. This is consistent with the general explanation of these two states since it is expected that the altered ion distribution is particularly relevant for defects.

Overall, k -imaging is a reproducible method for obtaining spatially resolved information about the dominant recombination pathways. In addition, two well-defined and meaningful measurement conditions were identified that provide insight into

open-circuit recombination in the dark and in the soaked steady-state. For practical reasons, i.e., to avoid extended soaking times, the dark is preferred over the soaked state as only this realistically offers fast, in-line applicable monitoring. In accordance, all data reported here are recorded using the dark-state procedure if not indicated otherwise.

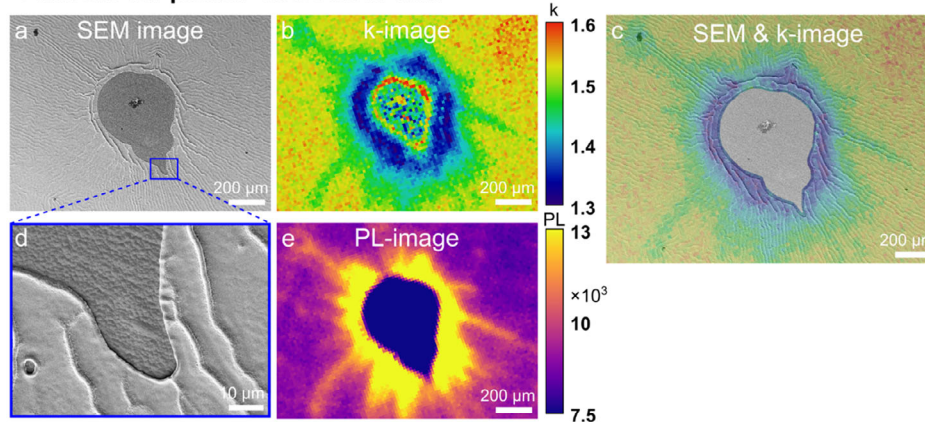
2.4 | Defect Detection

In the following, we present prime examples of how our method enables more insightful characterization by imaging the k -factor with high spatial resolution, in contrast to conventional PL imaging. The quality of perovskite thin-film absorbers can be affected by various defects, both in the bulk and at interfaces [49, 53]. The k -factor is a useful parameter to identify and measure the impact of these defects on carrier recombination as the underlying model is sensitive to both bulk and interface recombination. The method's capability to resolve defects is demonstrated by analyzing and correlating recorded PL and k -images with scanning electron microscopy (SEM) images of two common but severe macroscopic defects: a perovskite pinhole on a planar Si device and a sawing defect within a textured perovskite/Si device.

2.4.1 | Pinhole

First, a large pinhole in the perovskite layer, spin-coated on a planar Si device, is analyzed (Figure 4a–e). The SEM images (Figure 4a,d) display a distinct contrast between the exposed

Pinhole on planar Si bottom cell



Sawing-defect on textured Si bottom cell

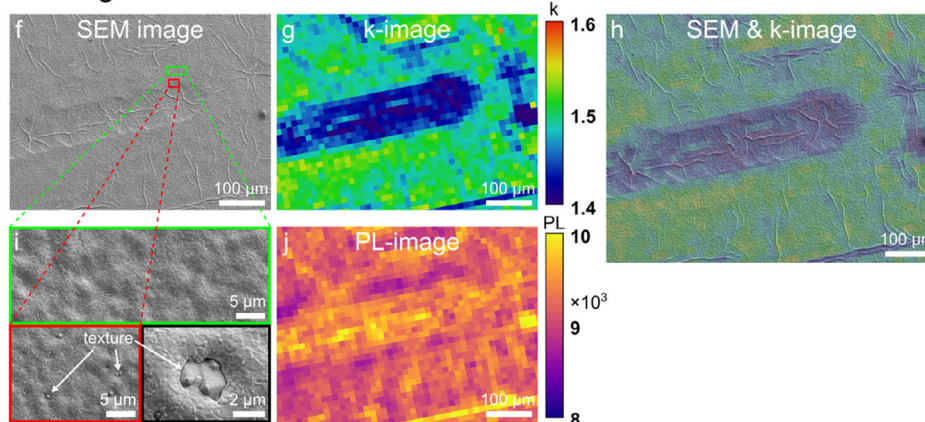


FIGURE 4 | Effects of critical processing defects such as (a–e) a pinhole in perovskite thin film on a planar silicon bottom cell and (f–j) a perovskite thin film processed on a textured silicon bottom cell showcased by k -images, photoluminescence (PL) images, and scanning electron microscopy (SEM) images. The merged images (c) and (h) correlate recombination with morphological information. The zoomed SEM inset in (d) shows a more detailed image of the perovskite wrinkles (blue) and (i) shows uncovered silicon pyramid tips at the boundary of the sawing defect (red and black) compared to the well-covered general surface (green).

inner area and the covered surroundings, with pronounced wrinkles near the boundary. At first sight, the k and PL images (Figure 4b,e) of the same section exhibit qualitatively similar shape and features. The PL image displays a clear distinction between the inner pinhole with expectably no PL, the wrinkles and boundary around the pinhole with increased PL, and the general surface further away with relatively homogeneous PL intensity. However, considering the apparent morphology variance between regions close to the pinhole and regions further apart, the absolute PL intensity is not suitable for a reliable analysis of the perovskite quality variation since it is drastically affected by the PL outcoupling. An illustrative example of an exclusively outcoupling related PL variation is presented in Figure S5a, Supporting Information. To enhance the visualization of the correlation between morphology and recombination degree, the k - and SEM images are superimposed (Figure 4c). The calculated k -factor inside the pinhole is not representative due to lack of perovskite and consequential lack of PL emission. The model fitting there is based on small amounts of reflected and refracted PL and camera noise, resulting in high variance and meaningless results. To avoid any misguidance, the inner region is excluded in the superimposed image. Outside the pinhole, we observe a strong correlation between a lowered

k -factor (~ 1.35) and more pronounced wrinkles near the edge of the pinhole, apart from any PL outcoupling effect. Similarly, some prominent radiating wrinkles show an effect on charge recombination with a k of approximately 1.45. At a greater distance, the wrinkle structure remains constant with no discernible deviation from the uniform sample, and the value of k also remains consistent at about 1.55. Overall, there is a trend, that enhanced wrinkling is associated with a decrease in k which is also supported by an equivalent defect illustrated in Figure S5b, Supporting Information. Although the origin of this shift in recombination cannot be fully explained without further analysis, two influences are discussed. Wrinkles are generally a sign of compressive stress relaxation during crystallization [54, 55]. Therefore, it is reasonable to assume that the extended wrinkle formation in the vicinity of the pinhole indicates different stress conditions compared to the uniform low-wrinkled surface. Unrelaxed stresses, whether compressive or tensile, are reported to facilitate the formation of crystal defects [54, 56]. These defects can lead to increased trap-assisted surface recombination, which is then reflected in a lowered k . Additionally, wrinkling causes local changes in layer thickness, resulting in an altered ratio between bulk and surface contributions.

2.4.2 | Wire-Sawing Defect

Second, a sawing defect on a textured Si device is discussed (Figure 4f–j), showing that even the impact on the perovskite film on textured substrates is detectable using *k*-imaging. Sawing defects are edges or trenches on the surface of pristine silicon wafers that occur during wire sawing [57]. While they are usually insignificant after the texture etching step, deep dents can remain detrimental and cause inhomogeneous or insufficient perovskite coverage. To demonstrate the general high quality of our perovskite material, we show the performance data of a representative unharmed textured tandem device in Figure S2, Supporting Information, having a PCE of 26.0%. Figure 4f–h displays a sawing defect covered with a perovskite thin film on a SEM image, along with the corresponding *k*-image and the superimposed image. The *k*-image shows lower values within the defect area, leading to a strong spatial correlation to the morphology represented by the SEM image. In contrast, while the PL image in Figure 4j shows a slight increase in absolute PL intensity inside the defect area, it is far less distinguishable from the unaffected surroundings. This pronounced decrease of *k*, with barely any sign in PL, is also observed on a larger scale, displayed in Figure S5c,d, Supporting Information. The PL image is certainly impacted by quality-independent effects since there are drastic morphological discontinuities around the defect. Similar to the pinhole example, *k* decreases to about 1.4 at the defect, while the surrounding demonstrates values between 1.5 and 1.55. The wrinkles inside the dent may contribute to the decrease in *k*. However, when compared to the wrinkles on the general surface, the effect is less spatially confined to wrinkles but instead fills the entire defect. Therefore, we expect that the primary contribution arises from a coverage-related issue, like a significant difference in perovskite layer thickness and microstructure. An indication that supports the argument of insufficient coverage is the observation of exposed silicon pyramids at the edge of these sawing defects. In contrast, the general surface is fully covered (see insets in Figure 4i). These uncovered areas behave like regular pinholes creating shunts in the device. Since the dimensions are in the single-micrometer range, there is no viable in-line method to detect them directly. Our method, however, can detect its impact on charge recombination.

To conclude, *k*-imaging is a sensitive technique that can identify and quantify the impact of defects and morphological inhomogeneities. It allows for assessing general layer quality as well as searching for specific deposition process-induced defects.

3 | Conclusion

While PL-based characterization methods are widely implemented in solar cell research, common methods like PL-imaging and PLQY either lack clarity in interpretation or are incompatible with large-area in-line applications due to their technical complexity. Photoluminescence, though, exhibits unique assets like noninvasive and contactless correlation with the implied V_{oc} and consequently absorber quality even in tandem solar cells. In order to overcome those restrictions and gain a robust and yet quantitative quality imaging method we extend the *k*-imaging method to usage of perovskite thin films in perovskite/Si tandem

solar cells. *k*-imaging enables local quality assessment of the perovskite thin-film absorber by extracting the effective parameter *k*, which gives insight into the competing recombination processes.

In this work, we demonstrate that *k*-imaging used for perovskite/Si tandem solar cells displays exceptional robustness against optical artifacts such as variations in the excitation and photon in- and out-coupling. The latter is especially relevant as this enables comparability for measurements of perovskite/Si tandem solar cells with varying stack composition and surface morphology, including roughness and in particular industrially relevant textures. Moreover, two repeatable but systematically distinct measurement states were described, namely dark and soaked, which are justified by ionic migration induced by light soaking. While the dark state is more practical in large-scale application due to its simplicity, both states yield valuable information for specific purposes. Lastly, by correlation with SEM measurements we proved that *k*-imaging is able to detect superficial as well as buried defects in the thin film, regardless of the Si bottom cell morphology. Pinholes and sawing defects, both being typical but also critical defects especially during optimization of new perovskite compositions and coating methods, are prominently identified. Overall, *k*-imaging is a valuable and versatile tool, suitable for application in both scientific optimization and industrial process monitoring.

4 | Methods

4.1 | Preparation of Hole Transport Layer

The preparation of the hole transport layers (HTL) is equal for all types of tandem cells. The substrates are (i) planar $25 \times 25 \text{ mm}^2$, (ii) textured $25 \times 25 \text{ mm}^2$ and (iii) textured $25 \times 25 \text{ mm}^2$ ITO/silicon bottom cells. The substrate is first washed by depositing isopropyl alcohol (IPA) (100 μL) and subsequently removing it by spin-coating (3000 rpm, 1000 rpm s^{-1} , 30 s). Afterwards, the substrates are dried on a 100°C hotplate for 10 min. The top half-stack is started with the deposition of NiO_x (15 nm) by RF sputtering onto the respective substrates at room temperature with a base pressure of $<3 \times 10^{-7}$ Torr, RF power of 100 W and argon flow rate of 18 sccm for 10 min. Then, 2PACz (0.5 mg mL^{-1}) solution in ethanol is deposited by spin-coating in a nitrogen glovebox at 3000 rpm for 30 s and annealed at 100°C for 10 min.

4.1.1 | Perovskite on Planar Substrate

M $\text{Cs}_{0.05}\text{FA}_{0.72}\text{MA}_{0.22}\text{Pb}(\text{I}_{0.77}\text{Br}_{0.23})_3$ Perovskite Precursor Solution Is Prepared, Dissolving a Mixture of PbI_2 , PbBr_2 , CsI, MABr and FAI in the Solvents DMF:DMSO (volume-Ratio Being 4:1). The Perovskite Layer Is Deposited by Spin-Coating in a Nitrogen Glovebox at 1000 rpm (200 rpm s^{-1}) for 10 s and 5000 rpm (2000 rpm s^{-1}) for 30 s. Then Ethyl Acetate (150 μL) as Antisolvent Is dropped 13 s before the End of the Second Step. Afterwards, the Perovskite Layers Were Annealed at 100°C for 30 min

4.1.2 | Level Perovskite on Textured Substrate

To fully cover the sub micrometer-sized pyramids, a 1.7 m $\text{Cs}_{0.05}\text{FA}_{0.72}\text{MA}_{0.22}\text{Pb}(\text{I}_{0.77}\text{Br}_{0.23})_3$ perovskite precursor solution

is prepared analogous to (i). The perovskite layers are deposited by spin-coating in a nitrogen glovebox at 400 rpm (400 rpm s^{-1}) for 3 s and 2000 rpm (2000 rpm s^{-1}) for 60 s, then ethyl acetate ($350 \mu\text{L}$) as antisolvent is dropped 5 s before the end of the second step. Afterwards, the perovskite layer is annealed at 100°C for 30 min.

4.1.3 | Conformal Perovskite on Textured Substrate

The perovskite thin film is fabricated using a scalable hybrid two-step deposition. Hereby the inorganics are deposited by evaporation in a first step, followed by a second inkjet-printing step, to deposit the organics. For the evaporated inorganic thin film, lead iodide and cesium-bromide are co-evaporated. For this, HTL-coated substrates are loaded into a CreaPhys evaporation system. Subsequently, lead iodide (200 nm , 1 Å s^{-1}) and cesium-bromide (20 nm , 0.1 Å s^{-1}) are evaporated. The standard recipe for the printed organic cation precursor used in this work contains FABr (39.8 mg mL^{-1}) and FAI (31.3 mg mL^{-1}) dissolved using a 9:1 volume ratio of n-butanol to IPA. A vortex shaker is used to dissolve the material. For inkjet printing, a Pixdro LP50 inkjet printer by SÜSS equipped with a Sapphire QS-256/10 AAA print head (10 pL) from SÜSS is used. By controlling the print head with a wave function that has the following parameters: width = $9 \mu\text{s}$, space = $5.7 \mu\text{s}$, level = 45.88 V , and rise = fall = $64.7 \text{ V } \mu\text{s}^{-1}$, an average droplet size of 10 pL is achieved. The organics are printed using a jetting frequency of 2 kHz and a resolution of $800 \text{ drops per inch (dpi)}$. Just before printing, the inorganic thin films are ejected from the nitrogen atmosphere. A vertical step size (in print head travel direction) of 10 and horizontal step size (perpendicular to the print head travel direction) of 10 is used. The printing process is done with a non-angled print head (native printing) toward the printing direction. After printing the organic cation precursor, the solar cells are annealed on a hot plate (150°C , 15 min) in ambient atmosphere (20°C , $40\text{--}45\%$ relative humidity). Afterwards, they are then stored in a nitrogen glove box.

4.2 | k-Imaging

Two 467 nm LED bars (LDL2-170/30-BL2, Creating Customer Satisfaction Inc.) powered by a power control unit (PD3-5024-4-EI, Creating Customer Satisfaction Inc.) excite the sample in a 45° symmetrical alignment. The tilt is introduced to ensure a homogeneous sample excitation and to reduce the detection of direct specular reflection. The image is recorded by a sCMOS camera (CS2100M-USB – Quantalux 2.1 MP Monochrome sCMOS Camera, Thorlabs) with a macro zoom lens (Zoom 7000, Navitar). To eliminate the detection of excitation light, a 695 nm absorptive long-pass filter (092 MRCIR – M550.0 \times 0.75, Schneider-Kreuznach) is attached to the lens. The camera system is located at a working distance of 130 mm , recording a top-view image with a variable detection window in between 8×6 and $48 \times 36 \text{ mm}^2$. Images are recorded within the full achievable excitation range, equivalent to $0.005\text{--}0.2$ suns, with linear step distribution. A background control with the image at zero excitation is performed to correct for stray light and the camera dark noise. The k -factor is extracted by fitting the intensity dependent, pixel-wise PL intensities with the model $I_{\text{PL}} \sim I_{\text{exc}}^k$. The total k is determined by spatially integrate

the PL-images and then perform the model fit. Due to the inversed procedure, the mean k (spatial average after pixelwise fitted k) is not equivalent to the total k .

4.3 | k-Factor Measurement Using PLQY Setup

Spectrally resolved PL measurements were taken using a commercial PLQY system (Quantum Yield Berlin, LuQy Pro). The excitation source is a 532 nm laser inside an integrating sphere in ambient air (relative humidity $\sim 30\%$). The excitation is swept logarithmically in a range between 0.005 and 0.2 suns, based on a J_{SC} of 19.24 mA cm^{-2} and EQE of 0.9 at the excitation wavelength. The PL emission is integrated for 2 s in the range between 640 and 840 nm . The effective excited step (soaking) time is $(4 \pm 0.2) \text{ s}$. k is fitted analogous to the k -imaging, by application of $I_{\text{PL}} \sim I_{\text{exc}}^k$.

4.4 | Scanning Electron Microscopy (SEM)

SEM analysis was carried out in a SEM (Zeiss LEO1530) with an in-lens detector and an aperture size of $30 \mu\text{m}$. The applied acceleration voltage for the surface analysis was 3 kV .

Acknowledgements

The authors gratefully acknowledge financial support by the Helmholtz Association via the Solar Technology Acceleration Platform (Solar TAP), the project Zeitenwende, the program-oriented funding phase IV (Materials and Technologies for the Energy Transition, Topic 1: Photovoltaics and Wind Energy, Code: 38.01.04), the German Federal Ministry for Economic Affairs and Climate Action (BMWK) through the projects SHAPE (03EE1123A) and 27Plus6 (03EE1056B), and the Karlsruhe School of Optics & Photonics (KSOP). Further, the authors would like to thank the Institute for Solar Energy Research (ISFH) for their cooperation and for providing silicon solar cells in the project 27Plus6. The “perovskite task force” at KIT is acknowledged for many fruitful discussions.

Open Access funding enabled and organized by Projekt DEAL.

Conflicts of Interest

The authors declare no conflicts of interest.

Data Availability Statement

The data that support the findings of this study are available from the corresponding author upon reasonable request.

References

1. S. Schafer and R. Brendel, *IEEE Journal of Photovoltaics* 8 (2018): 1156, <https://doi.org/10.1109/JPHOTOV.2018.2824024>.
2. C. Yang, W. Hu, J. Liu, et al., *Light: Science and Applications* 13 (2024): 227.
3. M. Jošt, L. Kegelmann, L. Korte, and S. Albrecht, *Advanced Energy Materials* 10 (2020): 1904102, <https://doi.org/10.1002/aenm.201904102>.
4. S. De Wolf, J. Holovsky, S. J. Moon, et al., *Journal of Physical Chemistry Letters* 5 (2014): 1035.

5. G. Xing, N. Mathews, S. Sun, et al., *Science* 342 (2013): 344, <https://doi.org/10.1126/science.1243167>.
6. M. Saliba, J. P. Correa-Baena, M. Grätzel, A. Hagfeldt, and A. Abate, *Angewandte Chemie International Edition* 57 (2018): 2554.
7. M. A. Green, E. D. Dunlop, M. Yoshita, et al., *Progress in Photovoltaics: Research and Applications* 32 (2024): 3.
8. S. W. Lee, S. Bae, D. Kim, and H. S. Lee, *Advanced Materials* 32 (2020): 2002202, <https://doi.org/10.1002/adma.202002202>.
9. X. Zhang, M. E. Turiansky, J. X. Shen, and C. G. Van De Walle, *Journal of Applied Physics* 131 (2022): 090901, <https://doi.org/10.1063/5.0083686>.
10. L. Fu, H. Li, L. Wang, R. Yin, B. Li, and L. Yin, *Energy and Environmental Science* 13 (2020): 4017.
11. D. B. Ritzer, T. Abzieher, A. Basibüyük, et al., *Progress in Photovoltaics: Research and Applications* 30 (2022): 360.
12. B. Abdollahi Nejand, D. B. Ritzer, H. Hu, et al., *Nature Energy* 7 (2022): 620.
13. R. Pesch, A. Diercks, J. Petry, et al., *Solar RRL* 8 (2024): 2470133, <https://doi.org/10.1002/solr.202400165>.
14. H. Eggers, F. Schackmar, T. Abzieher, et al., *Advanced Energy Materials* 10 (2020): 1903184, <https://doi.org/10.1002/aenm.201903184>.
15. F. Schackmar, F. Laufer, R. Singh, et al., *Advanced Materials Technologies* 8 (2023): 2201331, <https://doi.org/10.1002/admt.202201331>.
16. F. Laufer, S. Ziegler, F. Schackmar, et al., *Solar RRL* 7 (2023): 2201114, <https://doi.org/10.1002/solr.202201114>.
17. K. Geistert, S. Ternes, D. B. Ritzer, and U. W. Paetzold, *ACS Applied Materials & Interfaces* 15 (2023): 52519, <https://doi.org/10.1021/acsami.3c11923>.
18. A. Verma, D. Martineau, E. Hack, et al., *Journal of Materials Chemistry C* 8 (2020): 6124.
19. S. Ulična, B. Dou, D. H. Kim, et al., *ACS Applied Energy Materials* 1 (2018): 1853.
20. B. Tyagi, N. Kumar, H. B. Lee, et al., *Small Methods* 8 (2024): 2470010, <https://doi.org/10.1002/smtd.202300237>.
21. F. Wang, Y. Cao, C. Chen, et al., *Advanced Functional Materials* 28 (2018): 1803753, <https://doi.org/10.1002/adfm.201803753>.
22. E. Aydin, T. G. Allen, M. De Bastiani, et al., *Science* 383 (2024): eadh3849.
23. P. Zhu, C. Chen, J. Dai, et al., *Advanced Materials* 36 (2024): 2307357, <https://doi.org/10.1002/adma.202307357>.
24. C. H. Swartz, S. Paul, L. M. Mansfield, and M. W. Holtz, *Journal of Applied Physics* 125 (2019): 053103, <https://doi.org/10.1063/1.5064798>.
25. T. Kirchartz, J. A. Márquez, M. Stollerfoht, and T. Unold, *Advanced Energy Materials* 10 (2020): 1904134, <https://doi.org/10.1002/aenm.201904134>.
26. A. D. Bui, M. A. Mahmud, N. Mozaffari, et al., *Solar RRL* 5 (2021): 2100348, <https://doi.org/10.1002/solr.202100348>.
27. V. Sarritzu, N. Sestu, D. Marongiu, et al., *Scientific Reports* 7 (2017): 44629, <https://doi.org/10.1038/srep44629>.
28. P. Caprioglio, M. Stollerfoht, C. M. Wolff, et al., *Advanced Energy Materials* 9 (2019): 1901631, <https://doi.org/10.1002/aenm.201901631>.
29. B. Hacene, F. Laufer, S. Ternes, et al., *Advanced Materials Technologies* 9 (2023): 2301279, <https://doi.org/10.1002/admt.202301279>.
30. M. Stollerfoht, V. M. Le Corre, M. Feuerstein, P. Caprioglio, L. J. A. Koster, and D. Neher, *ACS Energy Letters* 4 (2019): 2887.
31. M. C. Schubert, L. E. Mundt, D. Walter, A. Fell, and S. W. Glunz, *Advanced Energy Materials* 10 (2020): 1904001, <https://doi.org/10.1002/aenm.201904001>.
32. N. Wu, Y. Wu, D. Walter, et al., *Energy Technology* 5 (2017): 1827.
33. G. El-Hajje, C. Momblona, L. Gil-Escrig, et al., *Energy & Environmental Science* 9 (2016): 2286.
34. K. Nguyen, O. Fischer, C. Messmer, et al., *Small* 20 (2024): 2403461, <https://doi.org/10.1002/smll.202403461>.
35. H. Shibata, M. Sakai, A. Yamada, et al., *Japanese Journal of Applied Physics, Part 1: Regular Papers and Short Notes and Review Papers* 44 (2005): 6113.
36. T. Schmidt, K. Lischka, and W. Zulehner, *Physical Review B* 45 (1992): 8989.
37. P. Calado, D. Burkitt, J. Yao, et al., *Physical Review Applied* 11 (2019): 044005, <https://doi.org/10.1103/PhysRevApplied.11.044005>.
38. P. Caprioglio, C. M. Wolff, O. J. Sandberg, et al., *Advanced Energy Materials* 10 (2020): 2000502, <https://doi.org/10.1002/aenm.202000502>.
39. C. M. Wolff, P. Caprioglio, M. Stollerfoht, and D. Neher, *Advanced Materials* 31 (2019): 1902762, <https://doi.org/10.1002/adma.201902762>.
40. J. Huang, Y. Yuan, Y. Shao, and Y. Yan, *Nature Reviews Materials* 2 (2017): 17042.
41. W. Shockley, *Bell System Technical Journal* 28 (1949): 435.
42. S. Bowden, V. Yelundur, and A. Rohatgi, Conference Record of the Twenty-Ninth IEEE Photovoltaic Specialists Conference (2002).
43. F. Babbe, L. Choubac, and S. Siebentritt, *Solar RRL* 2 (2018): 1800248, <https://doi.org/10.1002/solr.201800248>.
44. A. Delamarre, M. Paire, J. F. Guillemoles, and L. Lombez, *Progress in Photovoltaics: Research and Applications* 23 (2015): 1305.
45. A. Farag, R. Schmager, P. Fassel, et al., *ACS Applied Energy Materials* 5 (2022): 6700.
46. D. Mampallil and H. B. Eral, *Advances in Colloid and Interface Science* 252 (2018): 38.
47. J. M. Richter, M. Abdi-Jalebi, A. Sadhanala, et al., *Nature Communications* 7 (2016): 13941, <https://doi.org/10.1038/ncomms13941>.
48. Y. Chen, H. T. Yi, X. Wu, et al., *Nature Communications* 7 (2016): 12253, <https://doi.org/10.1038/ncomms12253>.
49. J. M. Ball and A. Petrozza, *Nature Energy* 1 (2016): 16149.
50. L. Lin, L. Yang, G. Du, et al., *ACS Applied Energy Materials* 6 (2023): 10303.
51. H. Choi, J. C. R. Ke, S. Skalsky, et al., *Journal of Materials Chemistry C* 8 (2020): 7509.
52. J. Liu, M. Hu, Z. Dai, W. Que, N. P. Padture, and Y. Zhou, *ACS Energy Letters* 6 (2021): 1003.
53. S. Agarwal, Pradeep R. Nair, and P. R. Nair, *Journal of Applied Physics* 122 (2017): 163104.
54. M. Dailey, Y. Li, and A. D. Printz, *ACS Omega* 6 (2021): 30214.
55. K. A. Bush, N. Rolston, A. Gold-Parker, et al., *ACS Energy Letters* 3 (2018): 1225.
56. T. W. Jones, A. Osherov, M. Alsari, et al., *Energy & Environmental Science* 12 (2019): 596.
57. G. Du, N. Chen, and P. Rossetto, *Semiconductor Science and Technology* 23 (2008): 055011, <https://doi.org/10.1088/0268-1242/23/5/055011>.

Supporting Information

Additional supporting information can be found online in the Supporting Information section.